Modeling the Gas Liquid Interface of Falling Film Reactors in Fully Developed Flow Regime

K. V. Muthukumar, M. Okraschevski, N. Bürkle, D. M. A. Bermudez, M. Haber, R. Koch, H.-J. Bauer, and C. Ates

Abstract In falling film reactors, the time scale of reaction is typically faster than the time scale of the mass transfer; hence the overall efficiency of the reactor is limited by the rate of mass transport to the reactive interface, which in turn depends on the effective surface area between the liquid phase and the gas phase. Therefore, the performance of these reactors strongly depends on how well the wavy interface dynamics and their influence on the reactive transport are understood at the most fundamental level. In this work, we focused on the numerical analysis of the wavy interface for alternative liquid distribution strategies with Smoothed Particle Hydrodynamics (SPH). In particular, we investigated the flow development in the entrance region and how it evolves into a fully developed region. We also analyzed the film statistics by extracting the probability density functions of the local film thicknesses in both time and frequency domains. Comparisons between SPH simulations and the available literature confirmed that the deployed numerical solution methodology can capture the global interface dynamics. However, higher residence times must be computed to fully capture the complex local mixing patterns in the fully developed region, which cannot be captured with periodic boundary conditions.

1 Introduction

The utilization of gas-liquid contact reactors is a popular strategy in the chemical industry for dealing with interfacial transport problems, such as passive cooling systems, gas cleaning units, and chemical absorbers. Depending on the physical and chemical properties of the gas and liquid phase, the operating conditions, and the reactor configuration, concentration profiles exhibit unique characteristics. For example, when the time scale for diffusion is much longer than the time scale for

K. V. Muthukumar · M. Okraschevski · N. Bürkle · D. M. A. Bermudez · M. Haber · R. Koch · H.-J. Bauer · C. Ates (✉)
Institut für Thermische Strömungsmaschinen KIT, Kaiserstraße 12, 76131 Karlsruhe, Germany
e-mail: cihan.ates@kit.edu

K. V. Muthukumar
e-mail: karthik.muthukumar@kit.edu

reaction (i.e., Hatta number (Ha) $>> 1$), as in the case of CO_2 chemical absorption, all the reactions occur within the film, and the yield is dictated by the effective interfacial area achieved per unit volume. In practice, it is possible to enhance the absorption process by a factor of 20 (on average) for the common CO_2 absorbents if the interface dynamics are properly tuned [16, 35]. Therefore, there lies a great opportunity to improve the reactor performance via engineering the gas-liquid interface, which in turn will smoothen the transition of novel technologies such as CO_2 capture in practice. Realization of this potential, however, requires a thorough understanding of the complex interface dynamics, including the transient film thicknesses, velocity distributions, and the simultaneous mass transfer process taking place in a very thin concentration boundary layer ($<$100 μm [19]).

The utilization of mathematical modeling to identify the coupled mass transfer and flow dynamics at gas-liquid interfaces has received significant attention, and it has a long history. The vanilla strategy in gas-liquid contact reactor modeling utilizes the enhancement factor (E) models dating back to the early 20th century. Since then, a variety of models have been developed for different gas-liquid mass transfer problems. The dependency of E on Ha is expressed differently depending on how the mass transfer dynamics are approximated, i.e., by using the film, penetration, and surface renewal theories [13]. Unfortunately, such simple models have been shown to fail to reproduce experimental measurements even for integrated (temporally and spatially averaged) CO_2 mass transfer rates for a variety of operating conditions [29]. Another simplifying approach exploited in the last couple of decades is the approximation of film dynamics analytically by combining the diffusion and reaction source terms via linearization or using empirical correlations [38], which also fails to mimic the dynamic nature of the interface [27].

A more comprehensive approach is the use of computational fluid dynamics (CFD) to analyze the mass transfer across the interface, as it has the potential to provide information on the coupled fluid dynamics and reactive transport across the film, which is not easily accessible from the experiments. In fact, the simultaneous solution of the two-phase Navier-Stokes and mass transfer equations is an active research field, yet the progress achieved so far has been limited compared to stand-alone free surface flow problems [5]. The challenges of reactive transport modeling stem from the large jumps in density, species concentration, and viscosity across the wavy liquid-gas interface. The corresponding prerequisites of the CFD approach then become (i) an accurate and sharp representation of the gas-liquid interface, (ii) the ability to capture discontinuities, local penetrations, and mixing of the phases, (iii) high temporal and spatial resolutions, (iv) easiness of incorporating chemical kinetics, (v) possibility to trace reaction fronts on top of the interface tracking and (vi) computational efficiency on parallel architectures.

Lagrangian methods offer an alternative to alleviate these issues, for which the SPH is a strong candidate. Noticeable recent examples with experimental validation related to the modeling of interfaces and wetting phenomena are the uphill movement of a liquid droplet over inclined surfaces [10], droplet wetting behavior on smooth and rough surfaces [21], flow through porous structures [2], rivulet dynamics on surfaces with different wettabilities [25], flow over micro-structured surfaces [22], droplet

flow on inclined structured surfaces [31], the impact of an oblate drop [34], low-speed impact force [39] and fluid-front instabilities in smooth and rough fractures [31]. The capabilities regarding the modeling of wetting phenomena have also been further extended very recently, particularly for the liquid film rupture [33] and super-hydrophilic surfaces [28]. With respect to the implementation of the mass transfer and the reaction kinetics, the SPH has been utilized for (i) modeling reactive transport and precipitation in a porous medium (via discretizing the diffusion-reaction equation) [24, 32], (ii) evaluating the concentration field of pollutants in a water tank (only diffusion) [3], (iii) CO_2 sequestration in porous media [4], (iv) multi-component mass transport in the Stefan tube [17], (v) phase separation in ternary mixtures [18], (vi) espresso extraction [14] and (vii) large particle dissolution under flow [30].

In the current work, our focus was mainly set on creating a virtual test rig to analyze the hydrodynamics of the gas-liquid interface, which is the very first step for the dimensioning of the large experimental test rig before its construction. For that purpose, SPH simulations were conducted using alternative liquid distributor designs in large-scale reactors to capture the transition from the entrance region to the fully developed region for the liquid phase. The results were compared with the available measurements to validate the methodology. Furthermore, practical concerns such as the effect of gas flow rate on the interface dynamics and possible simplifications in the solution domain for higher computational efficiency were discussed.

2 Numerical Method

In order to simulate the multiphase flow of air and the liquid film, the SPH method is used to solve the Navier-Stokes equations. The Lagrangian form of the continuity and momentum equation is required to derive the SPH schemes for calculating density ρ, velocity $\mathbf{v}$, volume forces f, shear stresses τ and static pressure p as a function of space and time t:

$$\frac{D\rho}{Dt} = -\rho\left(\nabla \cdot \mathbf{v}\right), \tag{1}$$

$$\rho\frac{D\mathbf{v}}{Dt} = -\nabla p + \nabla \cdot \tau + \rho\mathbf{f}. \tag{2}$$

In the present study, the mass of each particle is set constant, resulting in inherent mass conservation. A scheme as introduced by Espanol et al. [15] is used to compute the density field. The symmetric scheme is used to discretize the pressure gradient as it conserves linear momentum. Viscous forces are taken into account by following the formulation of Hu and Adam [20]. Following the weakly compressible approach, pressure is determined by means of the Tait equation with additional background pressure to avoid tensile instability [23]. Surface tension is represented

by the Continuum Surface Force model [1]. In all cases, particles are flagged by individual ID numbers, which offer the opportunity to track each particle inside the computational domain at each time step.

3 HPC Characteristics of the Code

The SPH code used for the present study is the recent version of the *turboSPH*, written in C++ and parallelized by means of MPI. Performance tests based on Allinea Performance Reports demonstrate that the implementation is dominantly compute-bound. The writing frequency is quite low, and file I/O is efficiently handled by using MPI I/O. As file I/O is not critical, the utilization of many computing nodes at a time is justified aiming for higher computational performance. The required memory per node is dominantly determined by the number of particles per MPI subdomain. The available memory per node is sufficient for the type of SPH predictions performed in this study.

The parallelization concept of the turboSPH code is based on a pure MPI implementation. In order to provide an equal load to each MPI process, the computational domain is statically decomposed during pre-processing. In the current two-phase simulations, all particles are evenly distributed in space, which greatly facilitates the partitioning of the domain. At the interfaces of all MPI subdomains, a classical ghost particle approach is used in order to communicate information between the different MPI processes. The domain decomposition begins with the creation of a bounding box around the complete computational domain. In the next step, the bounding box is split into smaller rectangular cuboids. Herein, each cuboid represents one MPI subdomain. Ideally, the process stops once all cuboids contain the same average number of particles per MPI process. It should also be noted that the underlying numerical approach is a particle-based method, and the neighbors of each particle are required at each time step to update scalar/vector quantities of interest. This is done by a list-search algorithm on a Cartesian background grid which shows a complexity of O(n).

Because the application is compute-bound, strong scaling is of primary importance for overall efficiency. In an earlier version of the code, the strong scalability was approximately 0.77 on 4000 cores, with an ideal behavior of 1. However, it was observed that the node-level performance was not optimal. Within the last few versions, several improvements were made, particularly in data management. It was changed from an array-of-structure to a structure-of-array architecture, which showed a more cache-friendly behavior. In accordance, the recent implementation allows the simulation of a larger physical time at the same computational resources than in the old versions, which is of critical importance for large-scale reactor simulations. In particular, the current code structure demonstrated superior performance compared to a commercial code and to an open-source code at the same computational configuration (Fig. 1), which enabled 30 fold increase in simulated physical time per invested CPU-hour [7]. It has been further demonstrated that the code can handle up to 10 billion particles and shows acceptable strong-scaling characteristics up to 10,000 cores [6, 8, 9, 11, 12].

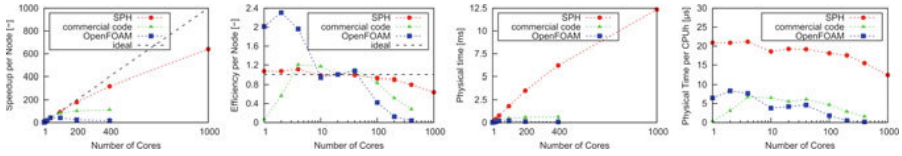

Fig. 1 Computational performance of the in-house developed SPH code. Test conditions: 1.5 million cells/particles, 1 h wall clock time, 2D geometry, two-phase flow

4 Computational Setup

The applicability of the outcomes of this work into practice strongly depends on how well the virtual test rig represents the real operating conditions. In accordance, we first looked into the expected film thicknesses as a function of liquid mass flow rate to determine the required spatial (hence temporal) resolution in the SPH domain. The Re number range for water is selected as 10–1000 to ensure a wavy flow regime for water (Kapitza (Ka) number >3800) [40]. The superficial gas velocity range is set as 1–10 cm/s, following the heuristics for gas-liquid contact reactors. From the available empirical correlations [26], the mean film thickness in the wavy region is found to be around 100 µm to 400 µm (it should be reminded that this value is likely to underestimate the true mean values in flat surfaces). Variations in the measured film thicknesses in time for similar flow conditions [36] further indicated that the instantaneous film thickness could be a couple of times larger than the mean value; hence instantaneous film thicknesses are expected to be between 100 and 1000 µm. Based on these heuristics, a mean liquid inlet velocity of 10 cm/s with an initial film thickness of 1 mm is set at the inlet boundary. Gas velocity was changed between 1 and 50 cm/s for alternative scenarios. In order to balance the requirements for high spatial resolution and the long simulation times, a spatial resolution of 50 µm was selected.

The exact wave characteristics cannot be known a priori; therefore, it is difficult to define the height of the virtual reactor to capture these wave dynamics. Nonetheless, as the wavelengths are expected to be less than 10 cm in $\mathrm{Re} = 100 - 1000$, we started with an effective reactor height of 20 cm, which was later extended up to 1 m height. Since the three-dimensional waves are chaotic in nature, we started with 2D systems to capture an ordered behavior, which is the very first step towards understanding the hydrodynamics of the wavy film flows.

With respect to the liquid distributors, we have tested three configurations shown in Fig. 2 as a starting point. In Case A, we assume to deploy a narrow-slit type distributor through which the solvent is fed. In Case B and C, we tested the effect of "film conditioning" on the evolution of the thin film flow.

All simulations were conducted with a temporal resolution of 14 MHz ($\Delta t \sim$ 70 ns), while the quantities of interest (positions, velocity components, pressure, density, fluid type, and unique particle IDs) were exported with a frequency of 250 Hz. Two-phase flow within the 20 and 100 cm height reactors were modeled

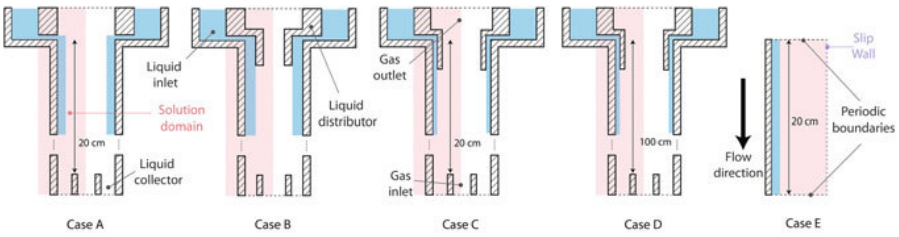

Fig. 2 2D reactors implemented in the SPH domain. Case A–C: short 20 cm reactors with different liquid distributor geometries, Case D: 100 cm reactor case, Case E: 20 cm reactor with periodic boundaries

for a simulated time of 6 and 14 s, respectively. The required computing times for the long reactor simulations were over one million CPU hours using around 1000 cores. The simulation has over 3 million particles per run, running for 1.8 million time steps at the same temporal resolution mentioned above (14 MHz). For periodic boundary conditions, the number of particles was cut-off to 4 hundred thousand. Therefore consuming only over half a million CPU hours and runs for 1.2 million time steps. The voluminous raw data is then post-processed to extract the local film thicknesses and velocity components at every stored time step. Data extraction is done by mounting "virtual probes" along the reactor, which record both the film thicknesses and velocity components.

5 Results and Discussions

5.1 Falling Film Dynamics in the Entrance Region

Our objectives in these virtual tests were (i) to investigate the transient nature of the wavy interface, (ii) to determine the time required for steady conditions, (iii) to find the height required to reach developed flow, and finally (iv) assess the effect of liquid distribution on the developing wavy interface. For that purpose, we first investigate the film dynamics at small reactor configurations with three different liquid distributor designs (Fig. 2).

The development of the local film thicknesses for all three cases is shown in Fig. 3. In all cases, it takes about 1 s to wet the reactor surface, where the initial wetting can be detected as a sudden increase in the film thicknesses. After the wetting, an oscillatory behavior was observed, which grows downstream of the liquid inlet. For the base case design (Case A), it is seen that there are some brief periods of time where the film thickness drops to zero (e.g., $t = 2.7$ s at 18 cm), indicating a partial wetting which is not desired. After reaching relatively steady conditions ($t>3$ s), partial wetting is still observed at around 5 s. Furthermore, the wavy film thickness profile still exhibits large local oscillations growing downstream. This is

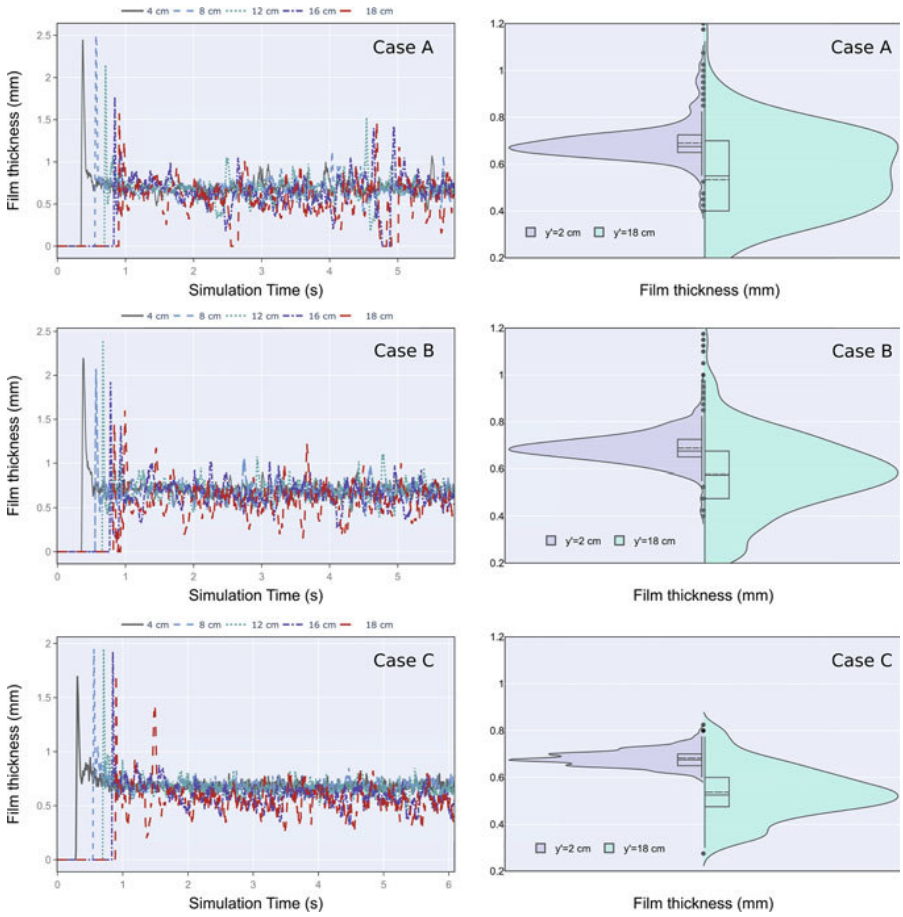

Fig. 3 Left: Temporal variations in falling film thicknesses for three different liquid distributors. Each curve represents the instantaneous film thickness at the given location, y. Right: PDFs of film thicknesses at different locations (statistics are derived for 3–6 s). Y-axis is in the direction of gravity

accompanied by a decrease in the mean film thickness as the film flows downstream. At the exit, the average film thickness was found to be around 0.52 mm. It should be noted that the model predictions on the average film thickness match perfectly with the experimental data [37] for the same Re number range.

In an attempt to overcome the growing instabilities and the partial surface wetting, we introduced better flow conditioning with a liquid distributor, for which the liquid thickness at the exit is set to be 1 mm and 0.5 mm respectively, to condition the film thickness to the expected range seen in Case A. As can be seen from Fig. 3, the reactor walls were completely wetted within the first second for both Case B and C. With the flow conditioning, however, flow stability has been increased noticeably, and the partial wetting problem in later times was alleviated completely. At a closer look,

fluctuations of film thickness at yb = 16 cm and y = 18 cm were even getting closer (i.e., converged) when we forced the film to flow through a gap of 0.5 mm (Case C). For both Case B and C, the deviations in the film thicknesses were also much smaller compared to Case A. In other words, with proper guidance of the downstream flow, it may be possible to reach the developed conditions at smaller residence times (hence reactor volumes).

We further looked into the film statistics by extracting the probability density functions (PDF) of the local film thicknesses at relatively stable conditions (Fig. 3, statistics are derived for $t > 3$ s). Close to the liquid distributor (y = 2 cm), the PDF has symmetric variation around a mean value (horizontal line in the box plot), yet we still observe the nucleation of additional waves, resulting in small hills at the higher end of the PDF. Herein, the largest peak can be considered as the film substrate thickness, while the width of the PDF is a measure of the film's waviness. As we go downstream of the reactor (Fig. 3, y = 18 cm), the width of the PDF broadens, i.e., multiple wave structures evolve. Towards the exit of the reactor, the mean film thickness is lowest, fluctuating at a much greater extent (i.e., box size) due to nonlinear combinations of multiple wave structures. When the film flow is modified with the distributor (Case B), it is seen that additional waves reflected as small hills at the upper end of the PDF at 2 cm are suppressed. More importantly, the flat PDF profile (Case A at 18 cm) is replaced by a curve, indicating a more dominant, single wave. When the liquid inlet is further conditioned with a narrower exit gap (Case C: gap width is set to expected averaged film thickness), the impact of the liquid distributor can be seen even very close to the inlet (at y = 2 cm), where the film thickness was forced to be narrower (0.5 mm, compared to the previous gap of 1 mm). Herein, the PDF function takes a much narrower distribution even at 18 cm downstream of the distributor exit. Moreover, the fluctuations in the film thickness were more symmetric and had a much smaller variance.

The hypothesis of multi-wave flow can be tested by transforming the wave signals into the frequency domain via Fast Fourier Transform (FFT), as shown in Fig. 4. Herein, the x-axis shows the spatial frequency of the individual waves, which explains the longitudinal spread. On the other hand, The y-axis gives the amplitude of the wave at a given frequency (i.e., power spectral density (PSD)). In the spectral coordinates, it is clearly seen that multiple large amplitude waves evolve at low frequencies along the reactor, which in turn leads to the flatter PDFs in the film thicknesses in Case A (Fig. 3). The PSD signals (Fig. 4) further reveal that the amplitude of the large peaks corresponding to the rolling waves gets smaller and more stable for Case B and C, whereas the spread of the lower frequency wave events gets even narrower for Case C. It is worth noting that a cascade of smaller amplitude capillary waves is visible in all cases.

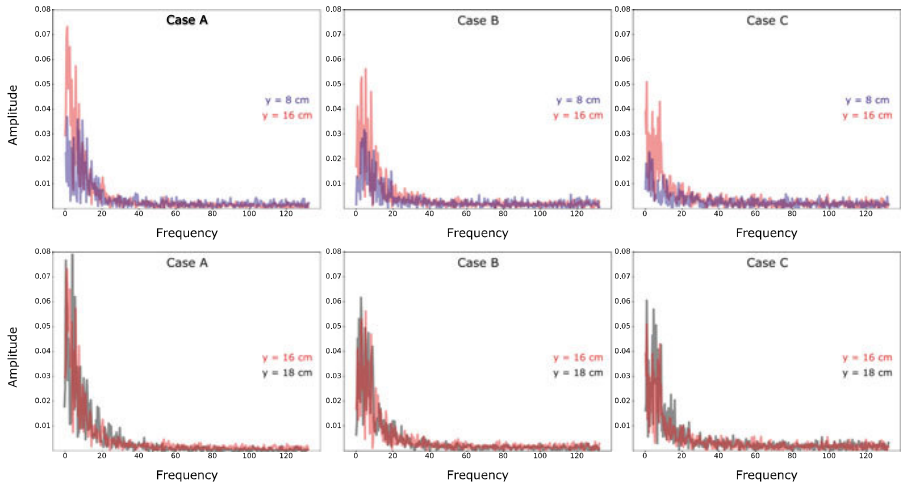

Fig. 4 Power spectrum density (PSD) for the film thicknesses in Case A, B and C. FFT is performed on film thickness profiles calculated between 3 and 6 s

5.2 Analysis of the Fully Developed Film Flow

The waviness of the thin film flow has been stabilized in 20 cm reactor configurations by conditioning the liquid film inlet. Nonetheless, the film flow dynamics have not been converged statistically yet along the reactor, which can be seen directly through the differences in the PSD curves at 12, 16, and 18 cm in all cases (Fig. 4). The film flow started to converge, yet 20 cm height was not sufficient to capture the developed region. In other words, there is a need to extend the simulated reactor height at least a couple of times to be sure of capturing the transition to the wavy developed flow. In accordance, Case C has been extended with a total reactor length of 100 cm as Case D (Fig. 2) to study the fully-developed film wave dynamics. Herein, the simulated time is extended to 14 s, with an increased liquid mass load ($= 3 * m_{liquid}$).

Figure 5 shows the variations in the film thickness in time at different reactor heights. One immediate observation is the extended range of the observed film thicknesses, which is 2–3 fold larger than the maximum value in a 20 cm reactor case. The wave dynamics are also much more complex than in the previous case, which can be attributed to the increased Re for the film flow. Another interesting observation at the meter scale reactor is the "droplet collisions". It is seen that liquid typically accumulates at the tip of the distributor plate, grows in size, and drips over the formed base liquid film (Fig. 6). Downstream of the distributor exit, these sliding droplets may further collide with previously dripped ones, creating a much larger droplet together. Such events are seen as large peaks in the virtual film thickness measurements. The occurrence of large peaks gets less prominent beyond 60 cm in the flow direction and is dispersed in the multiple wave structures discussed above. Nonetheless, such disturbance creates instabilities in the film, particularly in the first half section of the

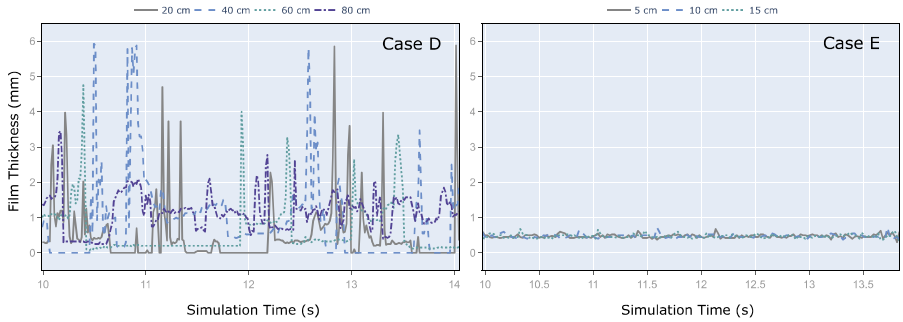

Fig. 5 Temporal variations in falling film thicknesses for the long reactor (Case D) and periodic boundary approximation (Case E). Each curve represents the instantaneous film thickness at the given location y

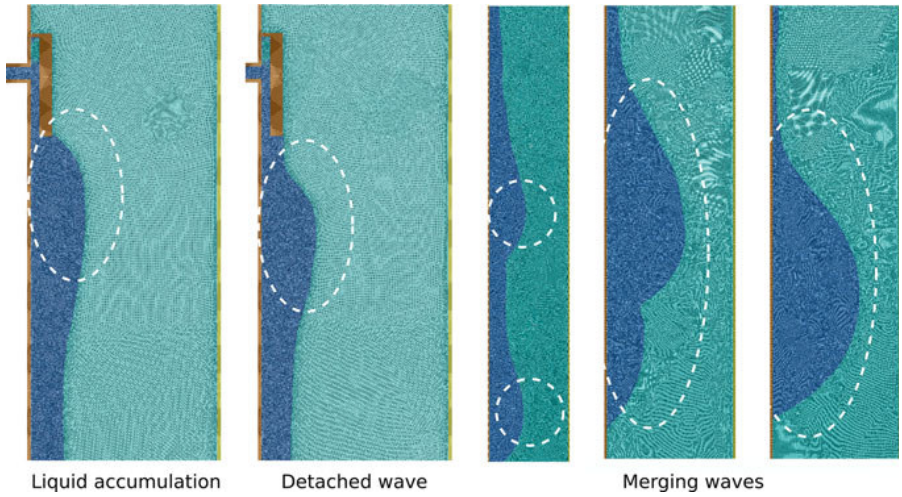

Fig. 6 Illustration of merging droplets along the liquid film. From left to right: accumulation of the liquid at the distributor, droplet detachment, droplet dripping over the base film, and merging surface waves

reactor, leading to partial wetting of the surface. It should be highlighted that such complex flow events could not be captured if the flow domain is small, underlining the need for conducting large-scale simulations to capture the effective surface area in the developed flow region.

Similar to Case A–C, the statistics of the film dynamics have been investigated with FFT in the long reactor for the latest three seconds time interval (Fig. 7, between 11 and 14 s). It is seen that both the low frequency-high amplitude and high frequency-low amplitude wave structures yield quite similar PSD signals. Beyond 60 cm, the wave structures do not change and yield almost identical scaling. The similarity gets much more visible when the PSD signals of 20 cm cases are compared to the 100 cm reactor configuration: the curves at y = 60 and 80 cm are much closer to one another

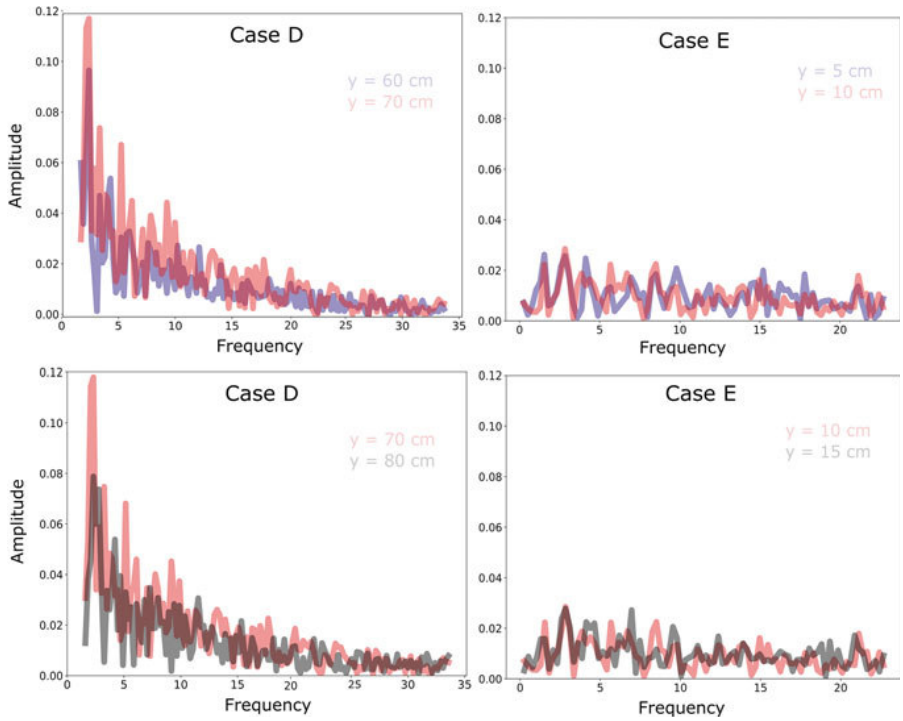

Fig. 7 Power spectrum density (PSD) for the film thicknesses in Case D and Case E. FFT is performed on film thickness profiles calculated between 11 and 14 s

than 16 and 18 cm of the shorter cases. This observation is of critical importance as it highlights the potential of HPC modeling of reactor configurations for system prototyping.

5.3 Predictive Accuracy of Periodic Boundary Conditions

One of the common practices in the modeling community is to deploy periodic boundary conditions to mimic large systems to reduce computational costs. In the case of falling film reactors, such simplifying assumptions is helpful as the computational cost mainly arises from the simulation time (order of at least seconds), which has to be reached with fine temporal and spatial resolutions (in the current study, time marching is performed in ns range with a spatial resolution of micrometers costing approximately 1 million CPU hours per case). In order to assess the predictive accuracy of periodic boundary assumption, Case D (100 cm) is used as a benchmark, and Case E (Fig. 2) is analyzed with respect to mean flow statistics for the same flow conditions. In the periodic case, the domain is discretized with the

same particle resolution, for which the simulation reached 14 s of physical time with 220,000 CPU hours (20% of the reference case).

Figure 5 shows the variations in film thickness for both the periodic boundary assumption (Case E) and the reference solution (Case D). The periodic approximation was found to smooth the complex flow structures along the developed region ($y > 60$ cm) and can only capture high-frequency (small) wave structures. The base film thickness remained the same throughout the simulation at around 0.5 mm, which was the initial film thickness passed as an initial condition. None of the complex events could be observed with the periodic boundaries.

The corresponding statistical variations in film dynamics are illustrated in Fig. 7. PSD analysis reveals that the periodic solution could not capture the high amplitude-low frequency waves (i.e., large waves) at all. Low-frequency components in the periodic case have the same amplitude as the capillary waves and the growth of large rolling waves could not be simulated. These comparisons indicate that we cannot afford to approximate the wavy gas-liquid interface with simplifying boundary conditions and need to resolve the whole interface.

6 Conclusion

- A virtual test rig in the SPH domain has been tailored for the gravity-driven thin film flow reactor under realistic flow conditions.
- Conditioning the flow with a distributor plate increased the flow stability and alleviated the partial wetting problem at small length scales.
- FFT analysis of the wavy interface at relatively steady conditions revealed that simple heuristics can underestimate the minimum reactor height to achieve developed flow conditions.
- The periodic boundary approximation could not capture the multiple wave structure that forms the gas-liquid interface. None of the low-frequency waves could be replicated with this simplifying assumption, underlining the need to fully capture the whole gas-liquid interface with open boundaries.
- Future work includes the analysis of developed multiple wave structures to construct low-order models and the assessment of the free surface flow approximation.

Acknowledgements This work was performed on the HoreKa supercomputer funded by the Ministry of Science, Research and the Arts Baden-Württemberg and by the Federal Ministry of Education and Research. The study is financially supported by the Friedrich and Elisabeth Boysen Foundation.

References

1. Adami, S., Hu, X.Y., Adams, N.A.: A new surface-tension formulation for multi-phase SPH using a reproducing divergence approximation. J. Comput. Phys. **229**(13), 5011–5021 (2010). https://doi.org/10.1016/j.jcp.2010.03.022
2. Aly, A.M., Asai, M.: Three-dimensional incompressible smoothed particle hydrodynamics for simulating fluid flows through porous structures. Transp. Porous Media **110**(3), 483–502 (2015). https://doi.org/10.1007/s11242-015-0568-8
3. Aristodemo, F., Federico, I., Veltri, P., Panizzo, A.: Two-phase SPH modelling of advective diffusion processes. Environ. Fluid Mech. **10**(4), 451–470 (2010). https://doi.org/10.1007/s10652-010-9166-z
4. Bandara, U.C., Palmer, B.J., Tartakovsky, A.M.: Effect of wettability alteration on long-term behavior of fluids in subsurface. Comput. Particle Mech. **3**(2), 277–289 (2016). https://doi.org/10.1007/s40571-015-0098-8
5. Bandi, P., Modigell, M., Groß, S., Reusken, A., Zhang, L., Heng, Y., Marquardt, W., Mhamdi, A.: On reduced modeling of mass transport in wavy falling films. AIChE J. **64**(6), 2265–2276 (2018). https://doi.org/10.1002/aic.16065
6. Braun, S.: Zur simulation der zerstäubung flüssigen kraftstoffs mit der smoothed particle hydrodynamics methode. Ph.D. thesis, Karlsruher Institut für Technologie (KIT) (2018)
7. Braun, S., Koch, R., Bauer, H.J.: Smoothed particle hydrodynamics for numerical predictions of primary atomization. In: Nagel, W.E., Kröner, D.H., Resch, M.M. (eds.) High Performance Computing in Science and Engineering'16, pp. 321–336. Springer International Publishing, Cham (2016)
8. Braun, S., Wieth, L., Holz, S., Dauch, T.F., Keller, M.C., Chaussonnet, G., Gepperth, S., Koch, R., Bauer, H.J.: Numerical prediction of air-assisted primary atomization using Smoothed Particle Hydrodynamics. Int. J. Multiph. Flow **114**, 303–315 (2019). https://doi.org/10.1016/j.ijmultiphaseflow.2019.03.008. http://www.sciencedirect.com/science/article/pii/S0301932218304087
9. Chaussonnet, G., Braun, S., Dauch, T., Keller, M., Sänger, A., Jakobs, T., Koch, R., Kolb, T., Bauer, H.J.: Toward the development of a virtual spray test-rig using the smoothed particle hydrodynamics method. Comput. Fluids **180**, 68–81 (2019). https://doi.org/10.1016/j.compfluid.2019.01.010. http://www.sciencedirect.com/science/article/pii/S0045793019300052
10. Das, A.K., Das, P.K.: Multimode dynamics of a liquid drop over an inclined surface with a wettability gradient. Langmuir **26**(12), 9547–9555 (2010). https://doi.org/10.1021/la100145e
11. Dauch, T., Ates, C., Rapp, T., Keller, M., Chaussonnet, G., Kaden, J., Okraschevski, M., Koch, R., Dachsbacher, C., Bauer, H.J.: Analyzing the interaction of vortex and gas-liquid interface dynamics in fuel spray nozzles by means of Lagrangian-coherent structures (2D). Energies **12**(13) (2019). https://doi.org/10.3390/en12132552
12. Dauch, T.F., Chaussonnet, G., Keller, M.C., Okraschevski, M., Ates, C., Koch, R., Bauer, H.J.: 3d predictions of the primary breakup of fuel in spray nozzles for aero engines. In: Nagel, W.E., Kröner, D.H., Resch, M.M. (eds.) High Performance Computing in Science and Engineering '20, pp. 419–433. Springer International Publishing, Cham (2021)
13. Doraiswamy, L.K., Uner, D.: Chemical reaction engineering: beyond the fundamentals, 1th ed. Taylor & Francis, New York (2014)
14. Ellero, M., Navarini, L.: Mesoscopic modelling and simulation of espresso coffee extraction. J. Food Eng. **263**(Dec. 2018), 181–194 (2019). https://doi.org/10.1016/j.jfoodeng.2019.05.038
15. Español, P., Revenga, M.: Smoothed dissipative particle dynamics. Phys. Rev. E **67**, 026705 (2003). https://doi.org/10.1103/PhysRevE.67.026705
16. Green, D.W., Perry, R.H.: Perry's Chemical Engineers' Handbook, 8th ed./edn. McGraw-Hill Education, New York (2008)
17. Hirschler, M., Säckel, W., Nieken, U.: On Maxwell-Stefan diffusion in smoothed particle hydrodynamics. Int. J. Heat Mass Transf. **103**, 548–554 (2016). https://doi.org/10.1016/j.ijheatmasstransfer.2016.07.061

18. Hopp-Hirschler, M., Baz, J., Hansen, N., Nieken, U.: Generalized Fickian approach for phase separating fluid mixtures in Smoothed Particle Hydrodynamics. Comput. Fluids **179**, 78–90 (2019). https://doi.org/10.1016/j.compfluid.2018.10.020
19. Hu, J., Yang, X., Yu, J., Dai, G.: Numerical simulation of carbon dioxide (CO2) absorption and interfacial mass transfer across vertically wavy falling film. Chem. Eng. Sci. **116**, 243–253 (2014). https://doi.org/10.1016/j.ces.2014.05.002
20. Hu, X.Y., Adams, N.A.: Angular-momentum conservative smoothed particle dynamics for incompressible viscous flows. Phys. Fluids **18**(10), 101702 (2006). https://doi.org/10.1063/1.2359741
21. Kordilla, J., Tartakovsky, A.M., Geyer, T.: A smoothed particle hydrodynamics model for droplet and film flow on smooth and rough fracture surfaces. Adv. Water Resour. **59**, 1–14 (2013). https://doi.org/10.1016/j.advwatres.2013.04.009
22. Lin, L., Sampath, R., Dinh, N.T., Akinci, N.: A computational study of thin film dynamics on micro-structured surfaces. In: ASME 2016 Heat Transfer Summer Conference, HT 2016, collocated with the ASME 2016 Fluids Engineering Division Summer Meeting and the ASME 2016 14th International Conference on Nanochannels, Microchannels, and Minichannels, vol. 2(June) (2016). https://doi.org/10.1115/HT2016-7382
23. Liu, M.B., Liu, G.R.: Smoothed particle hydrodynamics (SPH): an overview and recent developments. Arch. Comput. Methods Eng. **17**(1), 25–76 (2010). https://doi.org/10.1007/s11831-010-9040-7
24. Meakin, P., Tartakovsky, A.M.: Modeling and simulation of pore-scale multiphase fluid flow and reactive. Transport **47**(2008), 1–47 (2009). https://doi.org/10.1029/2008RG000263.1.INTRODUCTION. http://www.agu.org/pubs/crossref/2009/2008RG000263.shtml
25. Moghtadernejad, S., Jadidi, M., Dolatabadi, A., Esmail, N.: SPH simulation of rivulet dynamics on surfaces with various wettabilities. SAE Int. J. Aerosp. **8**(1), 160–173 (2015). https://doi.org/10.4271/2015-01-9005
26. Moran, K., Inumaru, J., Kawaji, M.: Instantaneous hydrodynamics of a laminar wavy liquid film. Int. J. Multiph. Flow **28**(5), 731–755 (2002). https://doi.org/10.1016/S0301-9322(02)00006-X. https://www.sciencedirect.com/science/article/pii/S030193220200006X
27. Norouzbahari, S., Shahhosseini, S., Ghaemi, A.: CO_2 chemical absorption into aqueous solutions of piperazine: modeling of kinetics and mass transfer rate. J. Natural Gas Sci. Eng. **26**, 1059–1067 (2015). https://doi.org/10.1016/j.jngse.2015.07.048
28. Olejnik, M., Pozorski, J.: A robust method for wetting phenomena within smoothed particle hydrodynamics. Flow Turbul. Combust. **104**(1), 115–137 (2020). https://doi.org/10.1007/s10494-019-00048-6
29. Putta, K.R., Tobiesen, F.A., Svendsen, H.F., Knuutila, H.K.: Applicability of enhancement factor models for CO_2 absorption into aqueous MEA solutions. Appl. Energy **206**(February), 765–783 (2017). https://doi.org/10.1016/j.apenergy.2017.08.173
30. Rahmat, A., Barigou, M., Alexiadis, A.: Numerical simulation of dissolution of solid particles in fluid flow using the SPH method. Int. J. Numer. Meth. Heat Fluid Flow **30**(1), 290–307 (2019). https://doi.org/10.1108/HFF-05-2019-0437
31. Shigorina, E., Tartakovsky, A.M., Kordilla, J.: Investigation of gravity-driven infiltration instabilities in smooth and rough fractures using a pairwise-force smoothed particle hydrodynamics model. Vadose Zone J. **18**(1), 1–12 (2019). https://doi.org/10.2136/vzj2018.08.0159
32. Tartakovsky, A.M., Trask, N., Pan, K., Jones, B., Pan, W., Williams, J.R.: Smoothed particle hydrodynamics and its applications for multiphase flow and reactive transport in porous media. Comput. Geosci. **20**(4), 807–834 (2016). https://doi.org/10.1007/s10596-015-9468-9
33. Xu, X., Dey, M., Qiu, M., Feng, J.J.: Modeling of van der Waals force with smoothed particle hydrodynamics: application to the rupture of thin liquid films. Appl. Math. Model. **83**, 719–735 (2020). https://doi.org/10.1016/j.apm.2020.03.003
34. Yang, X., Kong, S.C.: 3D simulation of drop impact on dry surface using SPH method. Int. J. Comput. Methods **15**(3), 1–23 (2018). https://doi.org/10.1142/S0219876218500111
35. Yoshimura, P.N., Nosoko, T., Nagata, T.: Enhancement of mass transfer into a falling laminar liquid film by two-dimensional surface waves-some experimental observations and modeling. Chem. Eng. Sci. **51**(8), 1231–1240 (1996). https://doi.org/10.1016/0009-2509(95)00387-8

36. Yu, Y., Wei, S., Yang, Y., Cheng, X.: Experimental study of water film falling and spreading on a large vertical plate. Prog. Nucl. Energy **54**(1), 22–28 (2012). https://doi.org/10.1016/j.pnucene.2011.09.007. https://www.sciencedirect.com/science/article/pii/S0149197011001892
37. Zadrazil, I., Matar, O.K., Markides, C.N.: An experimental characterization of downwards gas-liquid annular flow by laser-induced fluorescence: flow regimes and film statistics. Int. J. Multiph. Flow **60**, 87–102 (2014). https://doi.org/10.1016/j.ijmultiphaseflow.2013.11.008
38. Zahedi, G., Jahanmiri, A., Elkamel, A., Lohi, A.: Mathematical modeling, simulation, and experimental verification of CO_2 removal in a turbulent contact absorber. Chem. Eng. Technol. **29**(8), 916–922 (2006). https://doi.org/10.1002/ceat.200600005
39. Zhang, R., Zhang, B., Lv, Q., Li, J., Guo, P.: Effects of droplet shape on impact force of low-speed droplets colliding with solid surface. Exp. Fluids **60**(4), 1–13 (2019). http://dx.doi.org/10.1007/s00348-019-2712-7
40. Åkesjö, A., Gourdon, M., Vamling, L., Innings, F., Sasic, S.: Hydrodynamics of vertical falling films in a large-scale pilot unit - a combined experimental and numerical study. Int. J. Multiph. Flow **95**, 188–198 (2017). https://doi.org/10.1016/j.ijmultiphaseflow.2017.06.003. https://www.sciencedirect.com/science/article/pii/S0301932216307789